Supplementary Materials for

Observation of spin splitting effect in altermagnets CrSb

Ruiyue Chu[1,†], Xingkai Cheng[2,3,†], Xizhi Fu[2,3], Lei Han[1], Shixuan Liang[1], Yichen Su[1], Jiankun Dai[1], Yanzhang Cao[1], Weiqi Du[1], Feng Pan[1], Junwei Liu[2,3,*] and Cheng Song[1,*]

[1]Key Laboratory of Advanced Materials (MOE), School of Materials Science and Engineering, Tsinghua University, Beijing 100084, China.

[2]Department of Physics, The Hong Kong University of Science and Technology, Hong Kong 999077, China.

[3]IAS Center for Quantum Matter, The Hong Kong University of Science and Technology, Hong Kong, China

*Corresponding author. Email: liuj@ust.hk; songcheng@mail.tsinghua.edu.cn.

[†]These authors contributed equally.

Note 1. Symmetry analysis of spin conductivity in CrSb

In bulk CrSb, the crystal symmetry generators are given by $G = G_0 + M_z t \times G_0$ where $G_0 = \{E, C_3, M_x, I\}$. Among these, G_0 constrains the spin-resolved conductivity tensor for each spin channel, while $M_z t$ connects the conductivity tensors of the spin-up and spin-down channels. Specifically, the general form of the spin-resolved conductivity tensor is:

$$\sigma^{\uparrow(\downarrow)} = \begin{pmatrix} \sigma_{xx}^{\uparrow(\downarrow)} & \sigma_{xy}^{\uparrow(\downarrow)} & \sigma_{xz}^{\uparrow(\downarrow)} \\ \sigma_{xy}^{\uparrow(\downarrow)} & \sigma_{yy}^{\uparrow(\downarrow)} & \sigma_{yz}^{\uparrow(\downarrow)} \\ \sigma_{xz}^{\uparrow(\downarrow)} & \sigma_{yz}^{\uparrow(\downarrow)} & \sigma_{zz}^{\uparrow(\downarrow)} \end{pmatrix}$$

The symmetry constraints on the spin-resolved conductivity tensor are analyzed:

1. Under M_x, the following components vanish:

$$\sigma_{xy}^{\uparrow(\downarrow)} = \sigma_{yx}^{\uparrow(\downarrow)} = \sigma_{xz}^{\uparrow(\downarrow)} = \sigma_{zx}^{\uparrow(\downarrow)} = 0$$

   Thus, the conductivity tensor reduces to:

$$\sigma^{\uparrow(\downarrow)} = \begin{pmatrix} \sigma_{xx}^{\uparrow(\downarrow)} & 0 & 0 \\ 0 & \sigma_{yy}^{\uparrow(\downarrow)} & \sigma_{yz}^{\uparrow(\downarrow)} \\ 0 & \sigma_{yz}^{\uparrow(\downarrow)} & \sigma_{zz}^{\uparrow(\downarrow)} \end{pmatrix}$$

2. Under C_3, we have the constraints:

$$\sigma_{yy}^{\uparrow(\downarrow)} = \sigma_{xx}^{\uparrow(\downarrow)}, \sigma_{yz}^{\uparrow(\downarrow)} = \sigma_{zy}^{\uparrow(\downarrow)} = 0$$

   The tensor then simplifies to:

$$\sigma^{\uparrow(\downarrow)} = \begin{pmatrix} \sigma_{xx}^{\uparrow(\downarrow)} & 0 & 0 \\ 0 & \sigma_{xx}^{\uparrow(\downarrow)} & 0 \\ 0 & 0 & \sigma_{zz}^{\uparrow(\downarrow)} \end{pmatrix}$$

Note that $\sigma_{xx}^{\uparrow(\downarrow)} = \sigma_{yy}^{\uparrow(\downarrow)}$, indicates isotropic in-plane conductivity for both spin channels. Other symmetries such as identity E and inversion I impose no further constraints on the spin-resolved conductivity.

Further considering the symmetry $M_z t$ which enforces $\sigma_{xx}^{\uparrow} = \sigma_{xx}^{\downarrow}$ and $\sigma_{zz}^{\uparrow} = \sigma_{zz}^{\downarrow}$, the conductivity tensors for the spin-up and spin-down channels become:

$$\sigma^{\uparrow} = \begin{pmatrix} \sigma_{xx}^{\uparrow} & 0 & 0 \\ 0 & \sigma_{xx}^{\uparrow} & 0 \\ 0 & 0 & \sigma_{zz}^{\uparrow} \end{pmatrix}, \sigma^{\downarrow} = \begin{pmatrix} \sigma_{xx}^{\uparrow} & 0 & 0 \\ 0 & \sigma_{xx}^{\uparrow} & 0 \\ 0 & 0 & \sigma_{zz}^{\uparrow} \end{pmatrix}$$

Therefore, the spin-resolved conductivity tensor is:

$$\sigma^s = \frac{\hbar}{2e}\left(\sigma^{\uparrow} - \sigma^{\downarrow}\right) = \begin{pmatrix} 0 & 0 & 0 \\ 0 & 0 & 0 \\ 0 & 0 & 0 \end{pmatrix}$$

and the charge conductivity tensor is:

$$\sigma^c = \sigma^{\uparrow} + \sigma^{\downarrow} = \begin{pmatrix} \sigma_{xx}^c & 0 & 0 \\ 0 & \sigma_{xx}^c & 0 \\ 0 & 0 & \sigma_{zz}^c \end{pmatrix}$$

where $\sigma_{xx}^c = 2\sigma_{xx}^{\uparrow}, \sigma_{zz}^c = 2\sigma_{zz}^{\uparrow}$.

This shows that *g*-wave CrSb cannot support a spin current in its pristine state.

However, when C_3 is broken, following the same derivation procedure, we obtain:

$$\sigma^{\uparrow} = \begin{pmatrix} \sigma_{xx}^{\uparrow} & 0 & 0 \\ 0 & \sigma_{yy}^{\uparrow} & \sigma_{yz}^{\uparrow} \\ 0 & \sigma_{yz}^{\uparrow} & \sigma_{zz}^{\uparrow} \end{pmatrix}, \sigma^{\downarrow} = M_z^{-1}\sigma^{\uparrow}M_z = \begin{pmatrix} \sigma_{xx}^{\uparrow} & 0 & 0 \\ 0 & \sigma_{yy}^{\uparrow} & -\sigma_{yz}^{\uparrow} \\ 0 & -\sigma_{yz}^{\uparrow} & \sigma_{zz}^{\uparrow} \end{pmatrix}$$

The spin-resolved conductivity tensor then becomes:

$$\sigma^s = \frac{\hbar}{2e}\left(\sigma^{\uparrow} - \sigma^{\downarrow}\right) = \frac{\hbar}{2e}\begin{pmatrix} 0 & 0 & 0 \\ 0 & 0 & 2\sigma_{yz}^{\uparrow} \\ 0 & 2\sigma_{yz}^{\uparrow} & 0 \end{pmatrix}$$

and the charge conductivity tensor is:

$$\sigma^c = \sigma^{\uparrow} + \sigma^{\downarrow} = \begin{pmatrix} 2\sigma_{xx}^{\uparrow} & 0 & 0 \\ 0 & 2\sigma_{yy}^{\uparrow} & 0 \\ 0 & 0 & 2\sigma_{zz}^{\uparrow} \end{pmatrix}$$

Therefore, when an electric field is applied along the z-direction ($J^c \parallel [0001]$), a pure spin current is generated along the y-direction ($J^s \parallel [10\bar{1}0]$).

For clarity, we decompose the *g*-wave altermagnetic states connected by C_3 rotational symmetry into three *d*-wave Fermi surfaces, which allows us to analyze the three spin-conductivity tensors related by C_3 symmetry, as illustrated in Fig.S1. The total spin current can be decomposed into contributions from each Fermi surface:

$$\boldsymbol{J}_{tot}^s = \boldsymbol{J}_1^s + \boldsymbol{J}_2^s + \boldsymbol{J}_3^s,$$

where $\boldsymbol{J}_{tot}^s$ is the total spin current, and $\boldsymbol{J}_1^s$, $\boldsymbol{J}_2^s$ and $\boldsymbol{J}_3^s$ denote the spin currents originating from three Fermi surfaces, respectively. For example, the spin-conductivity tensor of the first Fermi surface (oriented along the y direction) is given by:

$$\sigma_1^s = \begin{pmatrix} 0 & 0 & 0 \\ 0 & 0 & \sigma_{yz}^s \\ 0 & \sigma_{yz}^s & 0 \end{pmatrix}.$$

Under C_3 symmetry, the two other equivalent conductivity tensors are obtained by rotating σ_1^s by $\frac{2\pi}{3}$ and $\frac{4\pi}{3}$ about the z-axis, respectively. For a rank-2 tensor, the transformation rule under a rotation by an angle θ follows $\sigma' = R(\theta) \cdot \sigma \cdot R^T(\theta)$, with rotation matrix as:

$$R(\theta) = \begin{pmatrix} \cos(\theta) & -\sin(\theta) & 0 \\ \sin(\theta) & \cos(\theta) & 0 \\ 0 & 0 & 1 \end{pmatrix},$$

and

$$C_3 = R\left(\theta = \frac{2\pi}{3}\right), C_3^2 = R\left(\theta = \frac{4\pi}{3}\right).$$

Applying these rotations yields the other two spin conductivity tensors:

$$\sigma_2^s = C_3 \cdot \sigma_1^s \cdot C_3^T = \frac{\sigma_{yz}^s}{2}\begin{pmatrix} 0 & 0 & -\sqrt{3} \\ 0 & 0 & -1 \\ -\sqrt{3} & -1 & 0 \end{pmatrix},$$

$$\sigma_3^s = C_3^2 \cdot \sigma_1^s \cdot (C_3^2)^T = \frac{\sigma_{yz}^s}{2}\begin{pmatrix} 0 & 0 & \sqrt{3} \\ 0 & 0 & -1 \\ \sqrt{3} & -1 & 0 \end{pmatrix}.$$

We then consider the spin currents arising from the three spin conductivity tensors. The applied electric field is expressed in spherical coordinates as:

$$\boldsymbol{E} = E(\sin\theta\cos\phi, \sin\theta\sin\phi, \cos\theta),$$

where E is the field magnitude, θ is the polar angle, and ϕ is the azimuthal angle. The spin current defined as $\boldsymbol{J}^s = \sigma^s \boldsymbol{E}$ is given by:

$$\boldsymbol{J}_1^s = \sigma_1^s \boldsymbol{E} = \sigma_{yz}^s E \begin{pmatrix} 0 \\ \cos\theta \\ \sin\theta\sin\phi \end{pmatrix},$$

$$\boldsymbol{J}_2^s = \sigma_2^s \boldsymbol{E} = \frac{\sigma_{yz}^s E}{2}\begin{pmatrix} -\sqrt{3}\cos\theta \\ -\cos\theta \\ -\sqrt{3}\sin\theta\cos\phi - \sin\theta\sin\phi \end{pmatrix},$$

$$\boldsymbol{J}_3^s = \sigma_3^s \boldsymbol{E} = \frac{\sigma_{yz}^s E}{2}\begin{pmatrix} \sqrt{3}\cos\theta \\ -\cos\theta \\ \sqrt{3}\sin\theta\cos\phi - \sin\theta\sin\phi \end{pmatrix}.$$

The total response $\boldsymbol{J}_{tot}^s$ is expressed as:

$$\boldsymbol{J}_{tot}^s = \boldsymbol{J}_1^s + \boldsymbol{J}_2^s + \boldsymbol{J}_3^s = \begin{pmatrix} 0 \\ 0 \\ 0 \end{pmatrix}.$$

To illustrate the cancellation mechanism explicitly, we evaluate the three contributions for electric fields aligned along the principal axes:

1. Electric field along the *z* direction ($\theta = 0$) (Figure S1a):

$$J_1^s = \sigma_{yz}^s E \begin{pmatrix} 0 \\ 1 \\ 0 \end{pmatrix}, J_2^s = \sigma_{yz}^s E \begin{pmatrix} -\frac{\sqrt{3}}{2} \\ -\frac{1}{2} \\ 0 \end{pmatrix}, J_3^s = \sigma_{yz}^s E \begin{pmatrix} \frac{\sqrt{3}}{2} \\ -\frac{1}{2} \\ 0 \end{pmatrix}$$

2. Electric field along the *x* direction ($\theta = \frac{\pi}{2}, \phi = 0$) (Figure S1b):

$$J_1^s = \sigma_{yz}^s E \begin{pmatrix} 0 \\ 0 \\ 0 \end{pmatrix}, J_2^s = \sigma_{yz}^s E \begin{pmatrix} 0 \\ 0 \\ -\frac{\sqrt{3}}{2} \end{pmatrix}, J_3^s = \sigma_{yz}^s E \begin{pmatrix} 0 \\ 0 \\ \frac{\sqrt{3}}{2} \end{pmatrix}$$

3. Electric field along the *y* direction ($\theta = \frac{\pi}{2}, \phi = \frac{\pi}{2}$) (Figure S1c):

$$J_1^s = \sigma_{yz}^s E \begin{pmatrix} 0 \\ 0 \\ 1 \end{pmatrix}, J_2^s = \sigma_{yz}^s E \begin{pmatrix} 0 \\ 0 \\ -\frac{1}{2} \end{pmatrix}, J_3^s = \sigma_{yz}^s E \begin{pmatrix} 0 \\ 0 \\ -\frac{1}{2} \end{pmatrix}$$

In every case, $\boldsymbol{J}_{tot}^s = \boldsymbol{J}_1^s + \boldsymbol{J}_2^s + \boldsymbol{J}_3^s = 0$. These results demonstrate the symmetry-enforced cancellation between C_3-connected Fermi surfaces. In contrast, breaking the C_3 symmetry disrupts this exact cancellation, giving rise to a nonzero spin response.

We now analyze the spin conductivity in the strained *g*-wave state, where the C_3 rotational symmetry is broken. In this configuration, we still introduce three spin conductivity tensors constrained by the remaining symmetries.

The first tensor, associated with the spin-surface oriented along the *y*-direction, is taken as

$$\sigma_1^s = \begin{pmatrix} 0 & 0 & 0 \\ 0 & 0 & \sigma_{yz}^1 \\ 0 & \sigma_{yz}^1 & 0 \end{pmatrix}$$

And the remaining two tensors, which are connected to each other by the mirror M_x, can be expressed as:

$$\sigma_2^s = \begin{pmatrix} 0 & 0 & \sigma_{xz}^2 \\ 0 & 0 & \sigma_{yz}^2 \\ \sigma_{xz}^2 & \sigma_{yz}^2 & 0 \end{pmatrix}$$

$$\sigma_3^s = M_x \cdot \sigma_2^s \cdot M_x^{-1} = \begin{pmatrix} 0 & 0 & -\sigma_{xz}^2 \\ 0 & 0 & \sigma_{yz}^2 \\ -\sigma_{xz}^2 & \sigma_{yz}^2 & 0 \end{pmatrix}$$

Consequently, under the electric filed $\boldsymbol{E} = E(\sin\theta\cos\phi, \sin\theta\sin\phi, \cos\theta)$, the spin currents are expressed as:

$$\boldsymbol{J}_1^s = \sigma_1^s E = E\begin{pmatrix} 0 \\ \sigma_{yz}^1 \cos\theta \\ \sigma_{yz}^1 \sin\theta \sin\phi \end{pmatrix},$$

$$\boldsymbol{J}_2^s = \sigma_2^s E = E\begin{pmatrix} \sigma_{xz}^2 \cos\theta \\ \sigma_{yz}^2 \cos\theta \\ \sigma_{xz}^2 \sin\theta\cos\phi + \sigma_{yz}^2 \sin\theta\sin\phi \end{pmatrix},$$

$$\boldsymbol{J}_3^s = \sigma_3^s E = E\begin{pmatrix} -\sigma_{xz}^2 \cos\theta \\ \sigma_{yz}^2 \cos\theta \\ -\sigma_{xz}^2 \sin\theta\cos\phi + \sigma_{yz}^2 \sin\theta\sin\phi \end{pmatrix},$$

With total spin current as:

$$\boldsymbol{J}_{tot}^s = \boldsymbol{J}_1^s + \boldsymbol{J}_2^s + \boldsymbol{J}_3^s = E\left(\sigma_{yz}^1 + 2\sigma_{yz}^2\right)\begin{pmatrix} 0 \\ \cos\theta \\ \sin\theta\sin\phi \end{pmatrix}$$

This result shows that a nonzero net spin current appears whenever the electric field has a component along the *y*- or *z*-direction, i.e., when $\cos\theta \neq 0$ or $\sin\theta\sin\phi \neq 0$.

To further illustrate why the spin currents are no longer canceled in the strained case, we explicitly derive the expressions for the three spin currents when the electric field is applied along three high-symmetry directions.

1. Electric field along the *z* direction ($\theta = 0$) (Figure S1d):

$$\boldsymbol{J}_1^s = E\begin{pmatrix} 0 \\ \sigma_{yz}^1 \\ 0 \end{pmatrix}, \boldsymbol{J}_2^s = E\begin{pmatrix} \sigma_{xz}^2 \\ \sigma_{yz}^2 \\ 0 \end{pmatrix}, \boldsymbol{J}_3^s = E\begin{pmatrix} -\sigma_{xz}^2 \\ \sigma_{yz}^2 \\ 0 \end{pmatrix},$$

and total spin current:

$$\boldsymbol{J}_{tot}^s = \boldsymbol{J}_1^s + \boldsymbol{J}_2^s + \boldsymbol{J}_3^s = E\begin{pmatrix} 0 \\ \sigma_{yz}^1 + 2\sigma_{yz}^2 \\ 0 \end{pmatrix} \neq 0.$$

2. Electric field along the *x* direction ($\theta = \frac{\pi}{2}, \phi = 0$) (Figure S1e):

$$\boldsymbol{J}_1^s = E\begin{pmatrix} 0 \\ 0 \\ 0 \end{pmatrix}, \boldsymbol{J}_2^s = E\begin{pmatrix} 0 \\ 0 \\ \sigma_{xz}^2 \end{pmatrix}, \boldsymbol{J}_3^s = E\begin{pmatrix} 0 \\ 0 \\ -\sigma_{xz}^2 \end{pmatrix},$$

and total spin current:

$$\boldsymbol{J}_{tot}^{s} = \boldsymbol{J}_{1}^{s} + \boldsymbol{J}_{2}^{s} + \boldsymbol{J}_{3}^{s} = \begin{pmatrix} 0 \\ 0 \\ 0 \end{pmatrix}.$$

3. Electric field along the *y* direction ($\theta = \frac{\pi}{2}, \phi = \frac{\pi}{2}$) (Figure S1f):

$$\boldsymbol{J}_{1}^{s} = E\begin{pmatrix} 0 \\ 0 \\ \sigma_{yz}^{1} \end{pmatrix}, \boldsymbol{J}_{2}^{s} = E\begin{pmatrix} 0 \\ 0 \\ \sigma_{yz}^{2} \end{pmatrix}, \boldsymbol{J}_{3}^{s} = E\begin{pmatrix} 0 \\ 0 \\ \sigma_{yz}^{2} \end{pmatrix},$$

and total spin current:

$$\boldsymbol{J}_{tot}^{s} = \boldsymbol{J}_{1}^{s} + \boldsymbol{J}_{2}^{s} + \boldsymbol{J}_{3}^{s} = E\begin{pmatrix} 0 \\ 0 \\ \sigma_{yz}^{1} + 2\sigma_{yz}^{2} \end{pmatrix} \neq 0.$$

Comparing these results with the unstrained case, where the C_3 symmetry enforces the relations $\sigma_{yz}^{2} = -\sigma_{yz}^{1}/2$, and $\sigma_{xz}^{2} = -\sqrt{3}\sigma_{yz}^{1}/2$—the sum of the three components would vanish identically. However, once C_3 symmetry is broken by strain, the tensor elements σ_{yz}^{1}, σ_{yz}^{2}, andσ_{xz}^{2} become independent variables, and consequently, the sum $\boldsymbol{J}_{1}^{s} + \boldsymbol{J}_{2}^{s} + \boldsymbol{J}_{3}^{s}$ is no longer forced to cancel, giving rise to a nonzero net spin current $\boldsymbol{J}_{tot}^{s}$. This analysis clearly demonstrates that symmetry breaking is the key mechanism that modulates spin transports and enables a non-zero spin current.

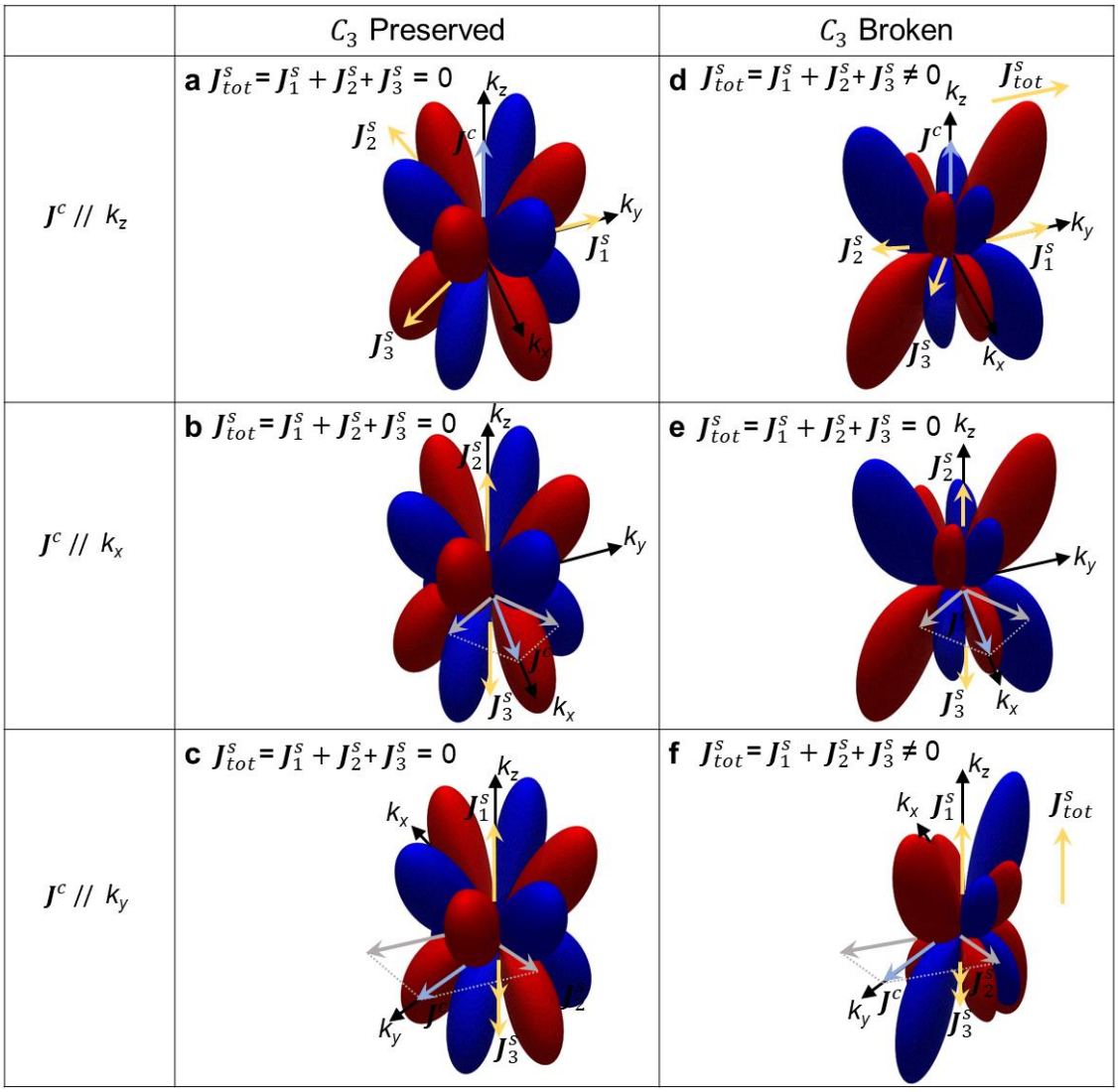

Fig. S1 Schematic illustration of spin-current generation in a *g*-wave altermagnet with preserved and broken C_3 symmetry. a-c, The charge current (J^c) is applied along the k_z (**a**), k_x (**b**), and k_y (**c**) directions, respectively, with C_3 symmetry preserved. **d-f,** The charge current is applied along the k_z (**d**), k_x (**e**), and k_y (**f**) directions, respectively, with C_3 symmetry broken. The blue and the yellow arrows represent the charge current and the spin current, respectively. The gray arrows indicate the components of the charge current. In the *g*-wave state with preserved C_3 symmetry, the net spin current vanishes, $J^s_{tot}=J^s_1+J^s_2+J^s_3=0$, regardless of the direction of the applied charge current. In contrast, in the *d*-wave-like state with broken C_3 symmetry, a finite net spin current is generated when the charge current is applied along the k_z and k_y directions.

Note 2. Sample growth and characterization

30 nm CrSb films with $(10\bar{1}0)$ and (0001)-orientations were grown by d.c. magnetron sputtering at 300 °C on GaAs(110) and GaAs(111) single crystalline substrates, respectively. The base pressure of the sputtering chamber was below 4×10^{-8} Torr. During deposition, the reaction sputtering atmosphere is Ar, with a sputtering pressure of 3 mTorr. The deposition speed, specified by X-ray reflectivity, was approximately 3 nm/min. To evaluate the crystallinity of the deposited CrSb films, conventional X-ray diffraction (XRD) analysis was performed, as illustrated in Fig. S2. XRD spectrum of GaAs(110)/CrSb($10\bar{1}0$) in Fig. S2a (top panel) shows a clear [$30\bar{3}0$] peak of CrSb. The ($30\bar{3}0$)-oriented CrSb is highly textured, as only one peak of CrSb is observed when the 2θ range from 20° to 100°. Figure S2a (lower panel) shows the XRD spectrum using non-oriented planes ($11\bar{2}0$), the ($11\bar{2}0$) and ($22\bar{4}0$) peaks can be observed in the 2θ range from 20° to 100°. In the case of the GaAs(111)/CrSb(0001) film (Fig. S2b), the CrSb(0002) and CrSb(0004) can be observed, confirming the high crystalline quality.

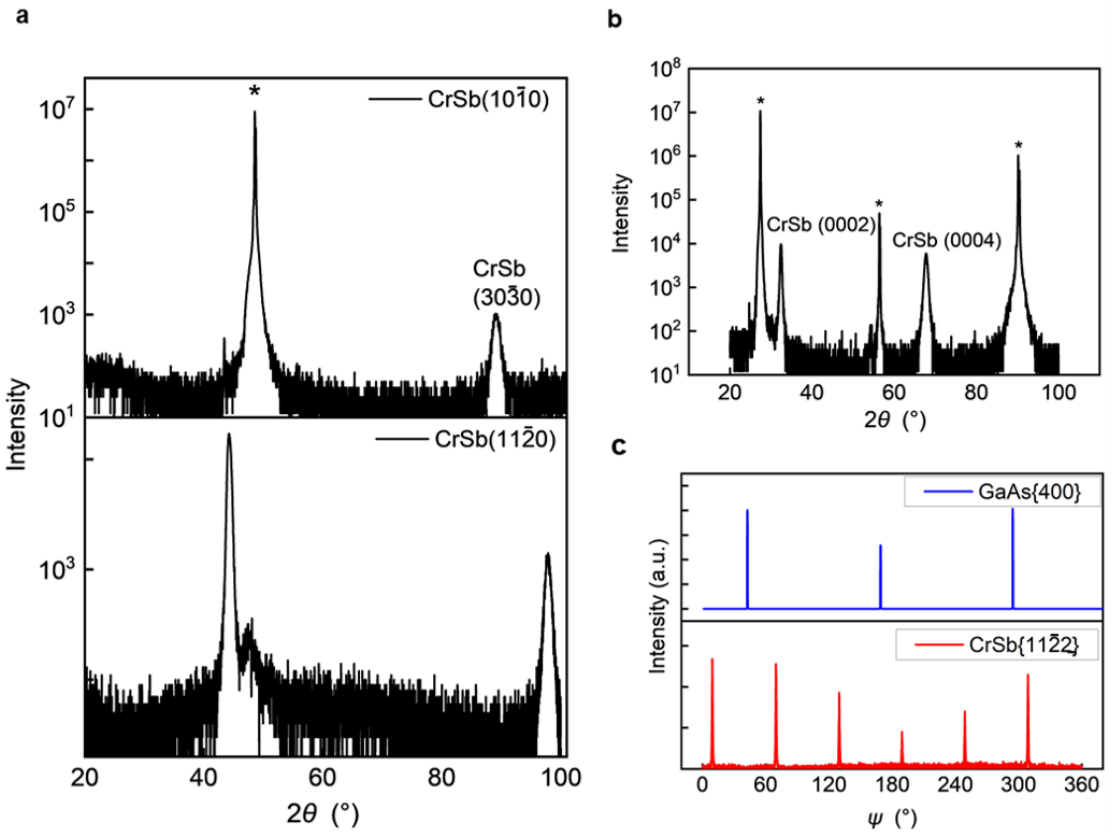

Fig. S2 XRD spectra of 30 nm-thick CrSb films grown on GaAs substrates. a, θ-2θ scan spectra of 30 nm GaAs(110)/CrSb(10$\bar{1}$0) film for the (10$\bar{1}$0)-oriented plane (top panel) and (11$\bar{2}$0)-non-oriented plane (lower panel). **b**, θ-2θ scan spectra of 30 nm GaAs(111)/CrSb(0001). **c**, ψ-scan spectra of CrSb(0001) films grown on the GaAs(111) substrate.

To verify the crystallography orientation between CrSb films and substrates, we performed ψ-scan XRD characterization. For GaAs(110)/CrSb(10$\bar{1}$0) film, both the CrSb film and substrate show two-fold symmetry, and the positions of their diffraction peaks are the same (Fig. 2b). It indicates that (10$\bar{1}$0)-oriented CrSb film shows epitaxy growth mode with the epitaxial relationship of CrSb(10$\bar{1}$0)[0001] // GaAs(110)[001], as illustrated in Fig. 2a in the main text. For GaAs(111)/CrSb(0001) film, the CrSb film shows three-fold symmetry and the substrate shows six-fold symmetry, the peak spacing of CrSb and GaAs is 30° (Fig. S2c). It indicates that (0001)-oriented CrSb film shows epitaxy growth mode with the epitaxial relationship of

CrSb(0001)[11$\bar{2}$0]//GaAs(111)[110], as illustrated in Fig. S3.

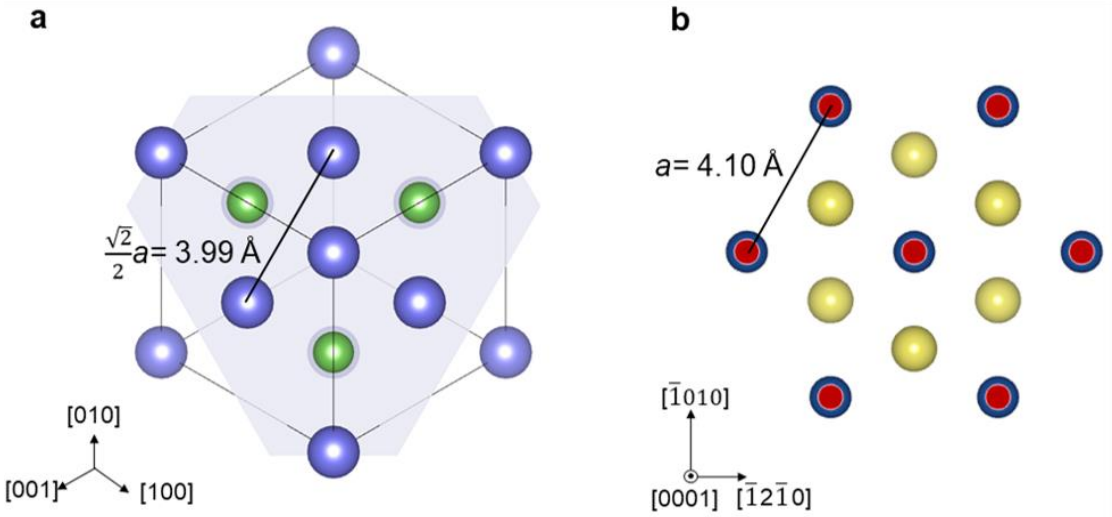

Fig. S3 Schematic of the epitaxy growth modes of CrSb(0001) film grown on GaAs(111) substrate. a, Schematic of the cubic GaAs(111) substrate, here $\frac{\sqrt{2}}{2}a$ = 3.99 Å. **b**, Schematic of the hexagonal CrSb(0001) film, here a = 4.13 Å.

Note 3. The *d*-wave-like Fermi surface in CrSb with C_3 symmetry breaking

The space group of bulk CrSb is the $P6_3/mmc$, with generators given by $G = \{E, C_{3z}, M_x, M_z t, I\}$. When antiferromagnetic (AFM) order is considered without spin–orbit coupling, the generators can be classified into two groups, expressed as $G = G_0 + C \times G_0$. Here $G_0 = \{E, C_{3z}, M_x, I\}$ denotes the symmetries that preserve the same AFM sublattice, while $C = M_z t$ represents the symmetry that exchanges the two AFM sublattices. In momentum space, G_0 constrains the Fermi surface for each spin channel, whereas $M_z t$ constrains the Fermi surfaces of the spin-up and spin-down channels, therefore, restricting spin conductivity for spin splitting torque (SST).

When C_3 symmetry is broken, the generators of G_0 reduce to $\{E, M_x, I\}$, while $M_z t$—which connects opposite AFM sublattices—is preserved, ensuring that CrSb remains a compensated antiferromagnet. A schematic illustration of the Fermi surface under this symmetry breaking is shown in Fig. 1f of the main text. To investigate strain effects in CrSb realistically, we performed first-principles calculations[1-4] based on the experimental lattice structure. The corresponding Fermi surface obtained from DFT is

shown in Fig. S4.

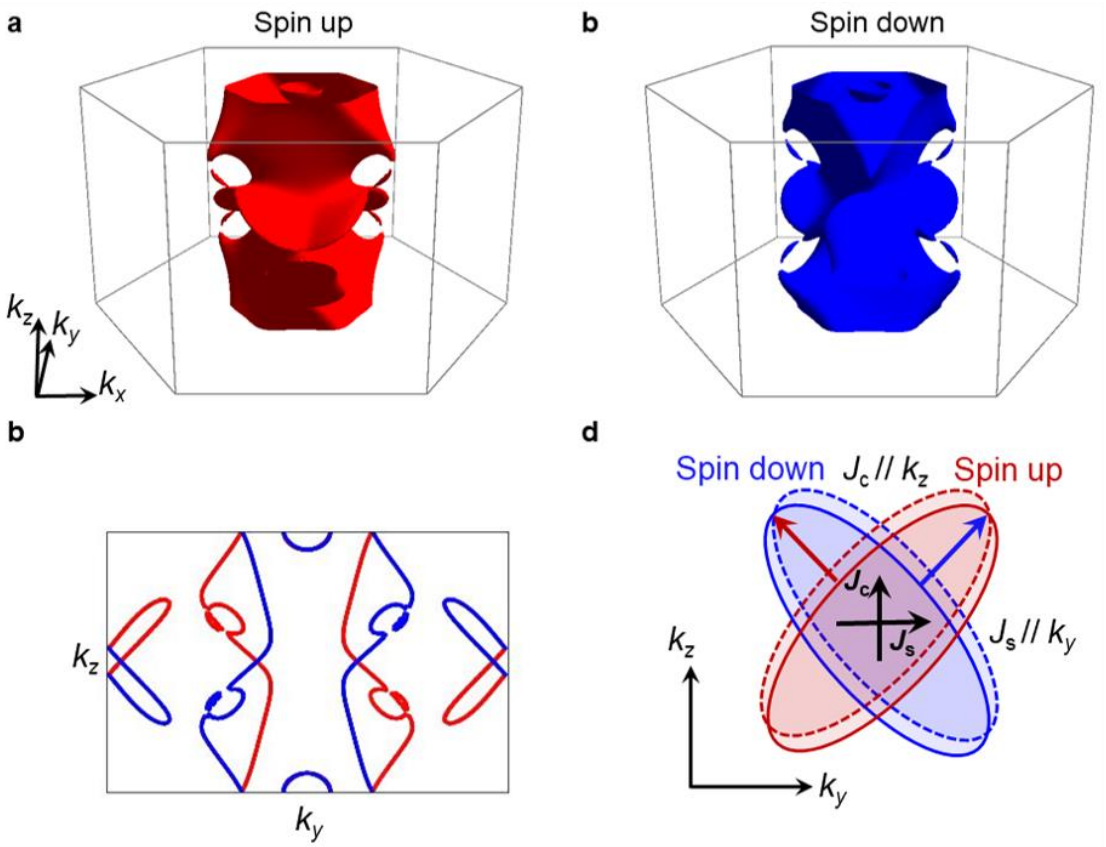

Fig. S4 Strained-induced Fermi surface under the breaking of C_3 symmetry. a,**b**, Spin-resolved Fermi surfaces for spin-up (**a**) and spin-down (**b**) channels. **c**, Cross-section of Fermi surface on $k_y - k_z$ plane. **d**, Spin splitting plane for charge-spin current interconversion.

Note 4. Spin conductivity in strained CrSb

We evaluate the spin-resolved conductivity by the Boltzmann equation using the Wannier model[5] derived from DFT calculations. The results are presented in Fig. S5, which shows that $\sigma_{yz}^{\downarrow} = -\sigma_{yz}^{\uparrow}$, while all other tensor elements remain identical between the two spin channels—consistent with our symmetry analysis. We further calculate the spin splitting angle via the relation:

$$\tan\theta_{ji}^{i} = \frac{2e}{\hbar}\frac{J^s}{J^c}$$

For strained CrSb under an electric field applied along the z-direction, this expression becomes

$$\tan\theta_{ji}^{i} = \frac{2e}{\hbar}\frac{J^{s}}{J^{c}} = \frac{2e}{\hbar}\frac{\sigma_{yz}^{s}E_{z}}{\sigma_{zz}^{c}E_{z}} = \frac{2e}{\hbar}\frac{\sigma_{yz}^{s}}{\sigma_{zz}^{c}}$$

Substituting $\sigma_{yz}^{s} = \frac{\hbar}{2e}2\sigma_{yz}^{\uparrow}$ and $\sigma_{zz}^{c} = 2\sigma_{zz}^{\uparrow}$, we obtain:

$$\tan\theta_{ji}^{i} = \frac{\sigma_{yz}^{\uparrow}}{\sigma_{zz}^{\uparrow}}$$

These calculation results are shown in Fig. 1f in the main text.

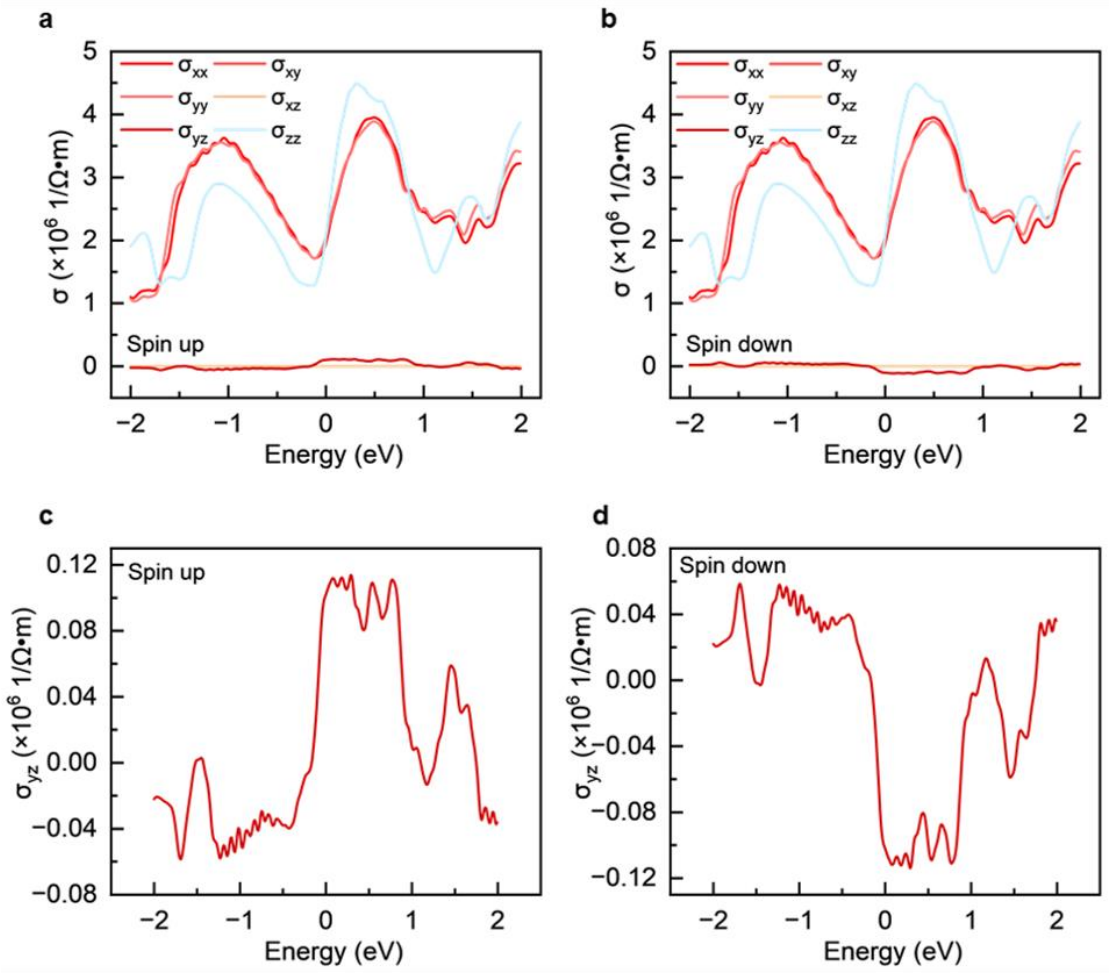

Fig. S5 Charge and spin-resolved conductivity components under the breaking of C_3. a,**b**, Spin-resolved conductivity for spin up $\sigma^{\uparrow}$ (**a**) and spin down $\sigma^{\downarrow}$ (**b**). **c**,**d**, σ_{yz}^{s} components corresponding to the experimental configuration for spin up (**c**) and spin down channels (**d**).

Note 5. Extracting σ_L in ST-FMR signals

The spin-torque ferromagnetic resonance (ST-FMR) voltages (V_{mix}) are composed

of torque signals from longitudinal spin polarization (σ_L), transverse spin polarization (σ_T), and out-of-plane spin polarization (σ_O), as shown in Table S1. The torque components acting on the Py moments can be categorized as follows: σ_L and σ_T generate field-like (FL) torques (τ_{FL}-σ_L and τ_{FL}-σ_T) and σ_O generates damping-like (DL) torque (τ_{DL}-σ_O), all of which contribute to out-of-plane torque ($\tau_\perp$). While σ_L and σ_T-induced damping-like torque (τ_{DL}-σ_L and τ_{DL}-σ_T) and σ_O-induced field-like torque (τ_{FL}-σ_O) constitute in-plane torque ($\tau_{//}$). In addition, the Oersted field provides an extra contribution to $\tau_\perp$. The current induced $\tau_{//}$ and $\tau_\perp$ contribute to the amplitudes of the symmetric (V_s) and antisymmetric (V_a) Lorentzian components of the V_{mix} line shape, respectively. Accordingly, these torque components can be extracted by fitting the V_{mix}-H curves to a superposition of V_s and V_a:[6-8]

$$V_{mix} = V_s F_s + V_a F_a \tag{S1}$$

$$F_s = \frac{\Delta H^2}{[(H - H_0)^2 + \Delta H^2]} \tag{S2}$$

$$F_a = \frac{\Delta H (H - H_0)}{[(H - H_0)^2 + \Delta H^2]} \tag{S3}$$

Where F_s and F_a are symmetric and antisymmetric Lorentzian functions and the amplitude of V_s and V_a can reflect the amplitude of the $\tau_{//}$ and $\tau_\perp$. H, ΔH, and H_0 are the external magnetic field, the spectral width, and the ferromagnetic resonance field, respectively. Based on Eqs. (*S*1)–(*S*3), the contributions of V_s and V_a can be extracted and shown in Fig.3b,c in the main text.

With respect to the expressions of τ_{DL} and τ_{FL} in Table S1, both τ_{DL}-σ_L, τ_{DL}-σ_T contribute to $\tau_{//}$, which is reflected in V_s. In materials where the longitudinal charge current produces spin current with only σ_T, V_{mix}, V_s and V_a change sign while maintaining the same amplitude at φ = 180°−β and 180°+β. φ is the angle between the current and the magnetization. To verify the presence of σ_L, we compare the ST-FMR signals obtained at magnetic field angles of 120° (180°−60°) and 240° (180°+60°). As depicted in Fig.3b,c, V_a(120°) and V_a(240°) have the same magnitude but opposite signs. However, V_s(120°) and V_s(240°) have different magnitudes, demonstrating there is the τ_{DL}-σ_L contribution. It should be emphasized that the damping-like torque and field-like torque have distinct physical origins. τ_{DL} component mainly stems from bulk effects,

such as the spin Hall effect, while τ_{FL} is typically generated by interfacial phenomena, for instance, the Rashba spin–orbit interaction. Because the SST in this system arises from the bulk CrSb layer, only the τ_{DL}-σ_L component contributes the measured V_s signals, but no τ_{FL}-σ_L component contributes V_a signals.

Table S1 Amplitudes of the symmetric (V_s) and antisymmetric (V_a) ST-FMR voltages are proportional to the SOT parallel ($\tau_{//}$) and vertical ($\tau_{\perp}$) to the sample plane, respectively. Note that the SOT in CrSb/Py bilayers is contributed by σ_L, σ_T, σ_O and Orested field.

	σ_L	σ_T	σ_O	Oersted field
$V_s(\tau_{//})$	Dampinglike	Dampinglike	Fieldlike	
	$(m \times \sigma_L \times m)$	$(m \times \sigma_T \times m)$	$(\sigma_O \times m)$	
$V_a(\tau_{\perp})$	Fieldlike	Fieldlike	Dampinglike	$-m \times H$
	$(\sigma_L \times m)$	$(\sigma_T \times m)$	$(m \times \sigma_O \times m)$	

Note 6. Angle-dependent ST-FMR measurements

To identify the exotic torques more accuracy, we performed angle-dependent ST-FMR measurement by changing the angle φ with an external magnetic field. Considering that V_{mix} contributed by σ_L and σ_T obey different angle-dependent lineshapes, that is, $\sin2\varphi\sin\varphi$ for σ_L and $\sin2\varphi\cos\varphi$ for σ_T, we can separate the contribution of σ_L and σ_T. The fitting curves for the angle-dependent ST-FMR signals are based on Eqs.(4) and (5):[9]

$$V_s = S_{DL}^{x}\sin\varphi \sin2\varphi + S_{DL}^{y}\cos\varphi \sin2\varphi + S_{FL}^{z}\sin2\varphi \quad (4)$$

$$V_a = A_{FL}^{x}\sin\varphi \sin2\varphi + A_{FL}^{y}\cos\varphi \sin2\varphi + A_{DL}^{z}\sin2\varphi \quad (5)$$

Where S_{DL}^{x}, S_{DL}^{y}, A_{DL}^{z} are the coefficients for the damping-like torques generated by the spin conductivities σ_L, σ_T and σ_O, respectively, while A_{FL}^{x}, A_{FL}^{y}, S_{FL}^{z} correspond to the field-like torque components. Noted that A_{FL}^{y} also incorporates the contribution from the Oersted-field. V_s components are analyzed in the main text, confirming the presence of τ_{DL}-σ_L in GaAs(110)/CrSb(10$\bar{1}$0)/Py films, which is a strain-induced SST.

Here we show the angle-dependent V_a signals of GaAs(110)/CrSb(10$\bar{1}$0)/Py films. V_a includes the contributions of τ_{FL}-σ_L, τ_{FL}-σ_T, τ_{DL}-σ_O, and the Oersted field. We extract the τ_{FL}-σ_L terms, sin2φcosφ, from V_a–φ curves, and their magnitudes are denoted as V_L. As depicted in Fig. S6a, when the current is applied along the CrSb[0001], the V_L is −0.13 μV (dark red curve), which is very small compared to the value in V_s–φ curves. Furthermore, the magnitudes of V_L remain minuscule regardless of the current is along any other crystal directions, such as [000$\bar{1}$], [$\bar{1}$2$\bar{1}$0] and [1$\bar{2}$10], as shown in Fig. S6b-d. These results demonstrate the absence of τ_{FL}-σ_L.

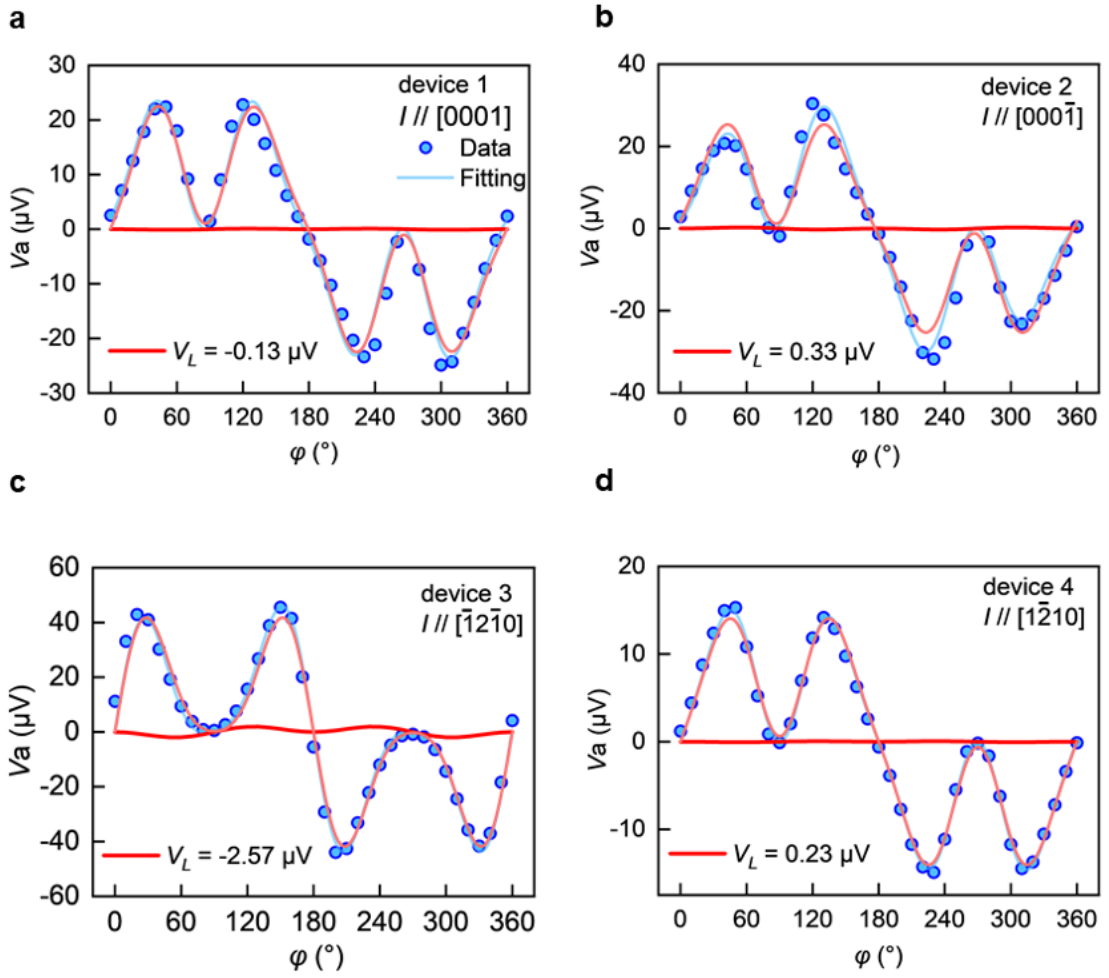

Fig. S6 Angle-dependent ST-FMR signals in GaAs(110)/CrSb(10 $\bar{1}$ 0)/Py. a-d, Antisymmetric resonance components (V_a) as a function of in-plane magnetic-field angle for a GaAs(110)/CrSb(10$\bar{1}$0)/Py film, with current applied along the [0001] (**a**), [000$\bar{1}$] (**b**), [$\bar{1}$2$\bar{1}$0](**c**), and [1$\bar{2}$10] (**d**).

To ensure the accuracy of the ST-FMR measurements, we grew a sample consisting of GaAs(111)/Cu(15 nm)/Py(9 nm) thin film (Fig. S7a). The 15 nm Cu layer cannot produce the spin current flow to the Py layer. Therefore, the V_s signal will be completely suppressed, and the V_a signal will present a sin2φcosφ component, which originates from the Oersted field. V_s and V_a components are extracted from V_{mix}, as shown in Fig. S7b-d. When the current is applied along the GaAs[001] (0°, Fig. S7b), only the V_a can be detected, and the V_s signal exhibits only minor fluctuations near the noise level. The angular dependence of the V_a component follows a sin2φcosφ dependence, indicating the absence of any spin-orbit or spin-splitting torque contributions. Similar behaviors are observed regardless of the applied current direction (120° or 240°). These results are consistent with the predictions, thereby validating both the reliability of our experimental setup and the robustness of the ST-FMR measurements.

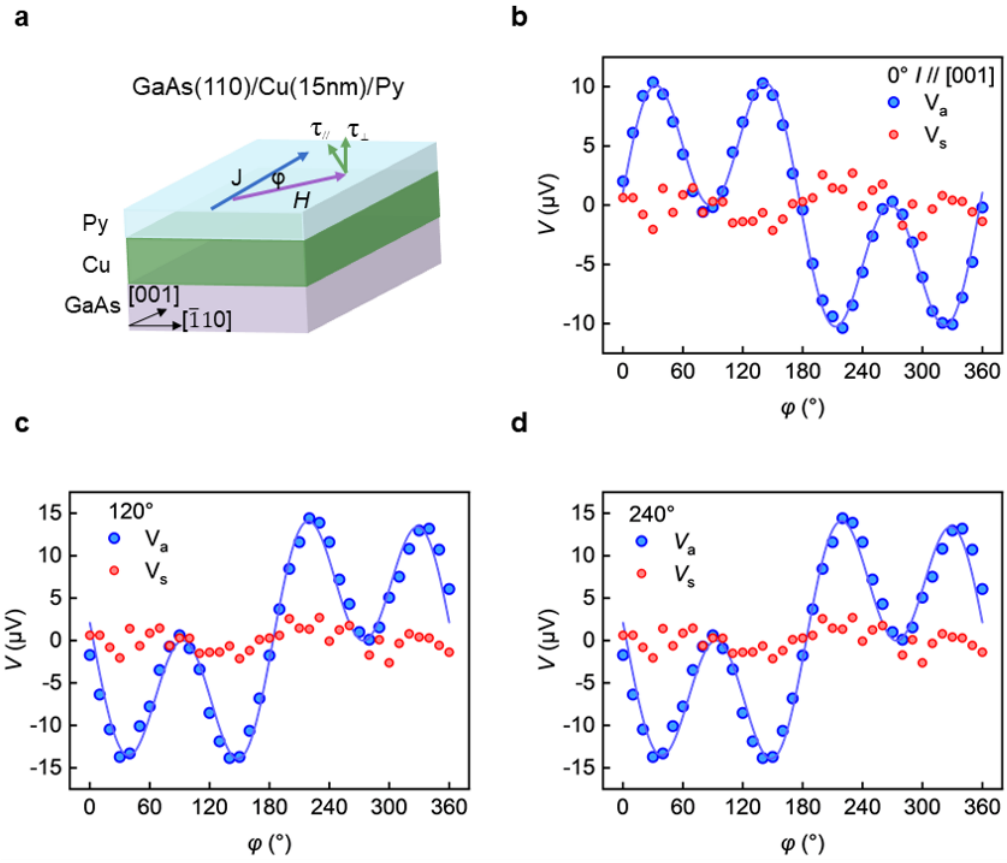

Fig. S7 Angle-dependent ST-FMR signals in GaAs(110)/Cu/Py. a, Schematic illustration of the GaAs(110)/Cu/Py thin film. **b-d**, V_a and V_s as a function of in-plane magnetic-field angle φ for a Cu(15 nm)/Py(9 nm) device, with current applied along

the GaAs[001] direction (0°, which is the angle between the current and the GaAs[001] direction) (**b**), 120° (**c**), and 240° (**d**).

Note 7. Magnetic properties of GaAs(110)/CrSb(10$\bar{1}$0)/Py

To calculate the spin splitting torque efficiency (θ_{ss}) of GaAs(110)/CrSb(10$\bar{1}$0)/Py films, we characterized the magnetic properties by the vibrating sample magnetometer, as shown in Fig. S8. The saturation magnetization of GaAs(110)/CrSb(10$\bar{1}$0)/Py films is $4\pi M_S$ ~7.2 kOe.

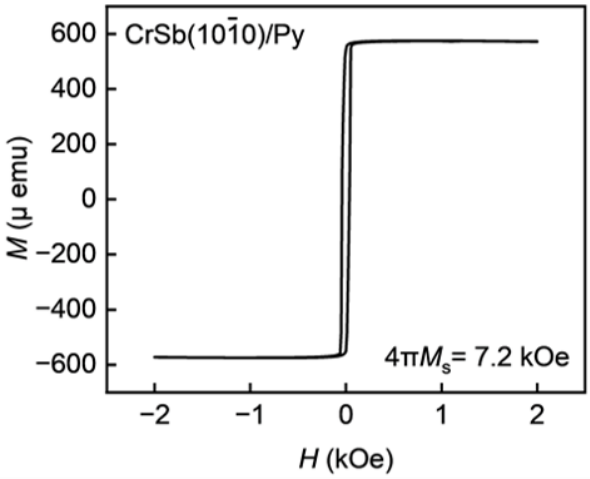

Fig. S8 Magnetic properties of GaAs(110)/CrSb(10 $\bar{1}$ 0)/Py. Dependence of magnetization (*M*) on in-plane *H* of GaAs(110)/CrSb(10$\bar{1}$0)/Py films.

The frequency-dependent V_{mix} signals and resonance field of GaAs(110)/CrSb(10$\bar{1}$0)/Py sample are shown in Fig. S9. As the frequency increases from 5 GHz to 13 GHz, the resonance fields increase, and the dependence of microwave frequency on the resonance fields is fitted by the Kittel equation:[6]

$$f = \frac{\gamma}{2\pi}\left(H_0\left(H_0 + 4\pi M_{eff}\right)\right)^{1/2} \quad (6)$$

Where *f* is the microwave frequency, γ is the gyromagnetic ratio, and the $4\pi M_{eff}$ is 6.07 kOe, which is obtained by fitting the Kittel equation.

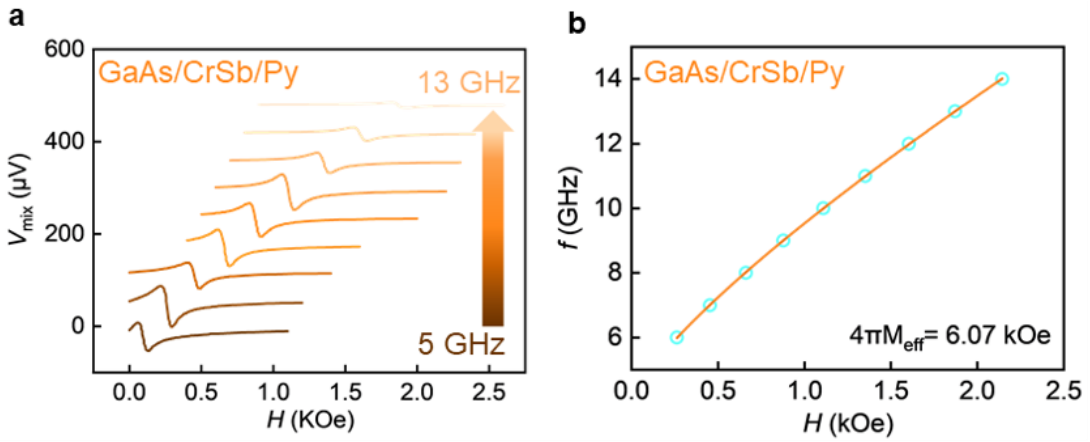

Fig. S9 Frequency-dependent ST-FMR measurements. a, V_{mix} signals with the frequency ranging from 5 GHz to 13 GHz for a GaAs(110)/CrSb(10$\bar{1}$0)/Py sample. **b**, Frequency-dependent resonance fields.

Note 8. Additional devices

In the main text, we demonstrated the strain-induced spin splitting torque τ_{DL}-σ_L in GaAs(110)/CrSb(10$\bar{1}$0)/Py films. Here, we further examine the repeatability of this effect using additional devices, as shown in Fig. S10. It is noteworthy that not all eight tested devices exhibit a pronounced σ_L spin polarization, which may be attributed to the partial cancellation of antiferromagnetic domains within the sample strip area. The V_a components display negligible V_L regardless of whether the current is applied along the [0001] or [000$\bar{1}$] (Fig. S10a and S10c), indicating a vanishingly small τ_{FL}-σ_L. When the current is applied along the CrSb[0001], the V_L is 4.87 μV, corresponding to V_L/V_T = 0.156 in V_s (Fig.S10b). This value is smaller than that of the device discussed in the main text, likely due to the influence of antiferromagnetic domain structures. When the current is applied along the [000$\bar{1}$], the V_L is −7.11 μV, yielding V_L/V_T = −0.30 in V_s (Fig.S10d), which is nearly identical in magnitude to the value reported in the main text. Taken together, these results confirm the repeatability and reliability of the strain-induced SST.

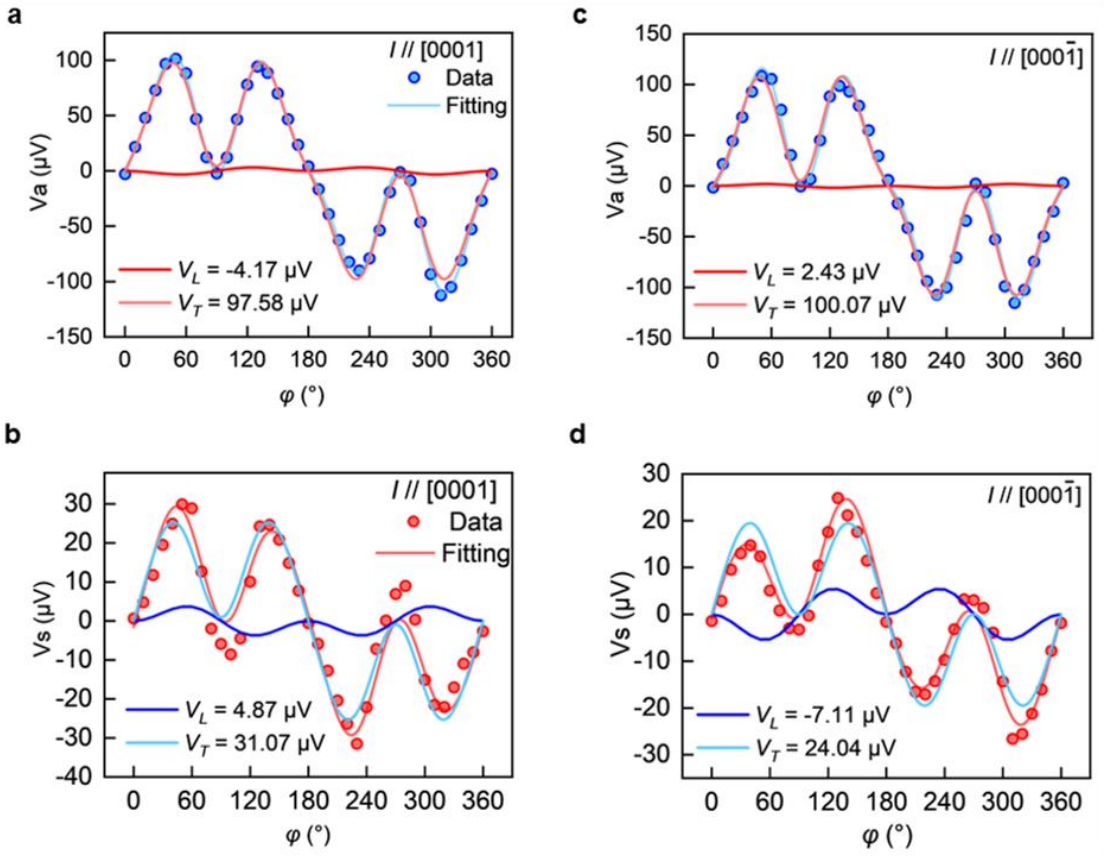

Fig. S10 Angle-dependent ST-FMR measurements in an additional GaAs(110)/CrSb(10$\bar{1}$0)/Py film. a-d, V_a and V_s as a function of φ, with current applied along the CrSb[0001] direction (**a**,**b**), and CrSb[000$\bar{1}$] (**c**,**d**).

Note 9. Characterization of spin-splitting torque in GaAs(111)/CrSb(0001)/Py

In the main text, we presented the V_a components when the current is applied along the CrSb[10$\bar{1}$0] and CrSb[$\bar{1}$2$\bar{1}$0] directions, demonstrating the absence of τ_{DL}-σ_O. Here, the corresponding V_s components are presented, from which the τ_{DL}-σ_O contribution, characterized by a sin2φ dependence, can be extracted from the V_s–φ curves, as presented in Fig. S11. The extracted V_O components are minimal with magnitudes of −0.24 μV when the current is applied along CrSb[10$\bar{1}$0], and −0.01 μV when the current is applied along CrSb[$\bar{1}$2$\bar{1}$0], confirming the absence of the τ_{FL}-σ_O. These results demonstrate that spin splitting torque cannot be generated in a system with preserved C_3 symmetry.

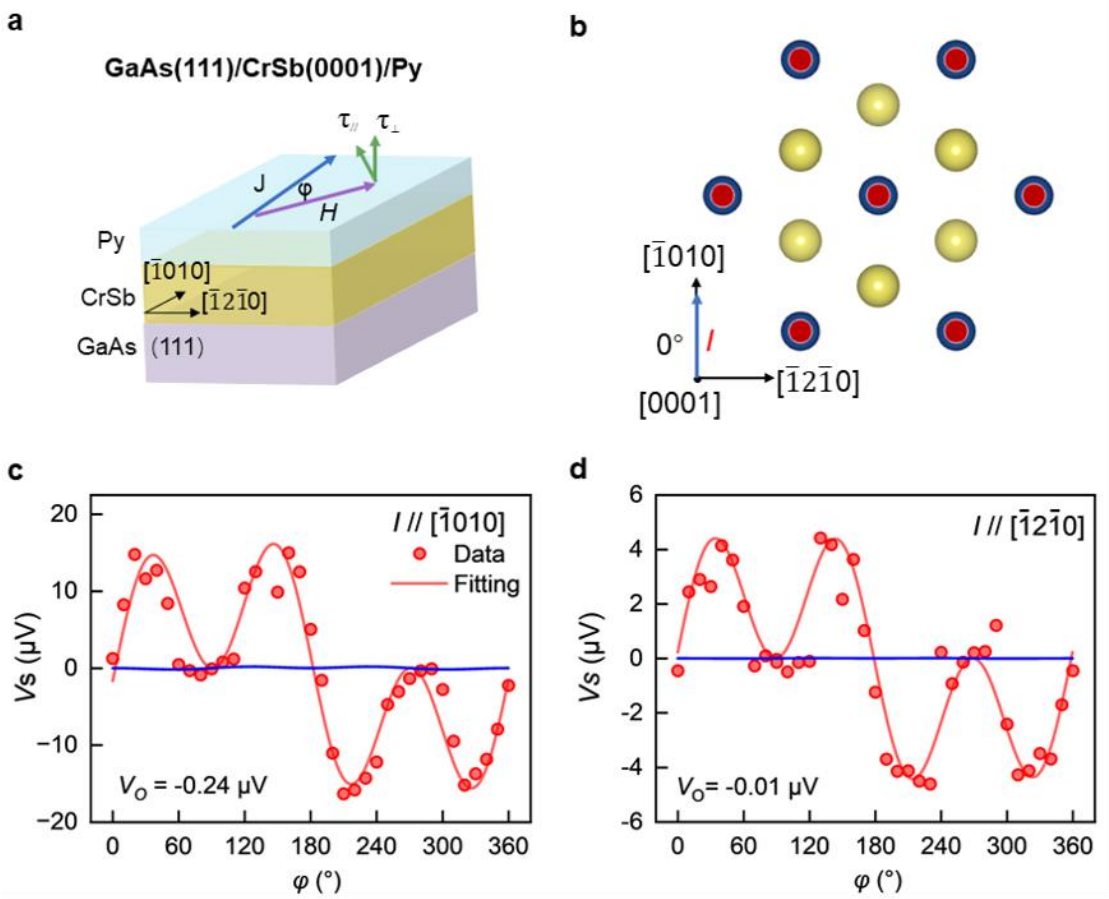

Fig. S11 Absence of SST in GaAs(111)/CrSb(0001)/Py film characterized by ST-FMR. a, The schematic of GaAs(111)/CrSb(0001)/Py film, where in-plane crystalline axes of the CrSb film are denoted. **b**, The CrSb(0001) plane and the crystal orientation. **c**,**d**, V_S as a function of φ, with current applied along the CrSb[$\bar{1}$010] (**c**), and CrSb[$\bar{1}2\bar{1}0$] (**d**).

References

1 Kresse, G. & Furthmüller, J. Efficiency of ab-initio total energy calculations for metals and semiconductors using a plane-wave basis set. *Comput. Mater. Sci.* **6**, 15–50 (1996).

2 Kresse, G. & Furthmüller, J. Efficient iterative schemes for ab initio total-energy calculations using a plane-wave basis set. *Phys. Rev. B* **54**, 11169–11186 (1996).

3 Perdew, J. P., Burke, K. & Ernzerhof, M. Generalized Gradient Approximation Made Simple. *Phys. Rev. Lett.* **77**, 3865–3868 (1996).

4 Kresse, G. & Joubert, D. From ultrasoft pseudopotentials to the projector augmented-wave method. *Phy. Rev. B* **59**, 1758–1775 (1999).

5 Mostofi, A. A. *et al.* wannier90: A tool for obtaining maximally-localised Wannier functions. *Comput. Mater. Sci.* **178**, 685–699 (2008).

6 Liu, L., Moriyama, T., Ralph, D. C. & Buhrman, R. A. Spin-Torque Ferromagnetic Resonance Induced by the Spin Hall Effect. *Phys. Rev. Lett.* **106**, 036601 (2011).

7 Fang, D. *et al.* Spin–orbit-driven ferromagnetic resonance. *Nat. Nanotechnol.* **6**, 413–417 (2011).

8 MacNeill, D. *et al.* Control of spin–orbit torques through crystal symmetry in WTe2/ferromagnet bilayers. *Nat. Phys.* **13**, 300–305 (2017).

9 Bose, A. *et al.* Tilted spin current generated by the collinear antiferromagnet ruthenium dioxide. *Nat. Electron.* **5**, 267–274 (2022).